Experimental Techniques
https://doi.org/10.1007/s40799-023-00628-2

RESEARCH PAPER

A Non-Intrusive Fluorescent Pattern for Internal Microscale Strain Measurements Using Digital Image Correlation

L. A. Ahure Powell[1] · W. D. Mulhearn[1,2] · S. Chen[3,4] · S. J. Stranick[3] · J. W. Gilman[1,5] · M. A. Iadicola[1] · J. W. Woodcock[1]

Received: 22 July 2022 / Accepted: 16 January 2023

Abstract

A non-intrusive internal fluorescent pattern is designed, developed, and tested using digital image correlation (DIC) to measure deformation at internal planes of a polymer matrix material. This new patterning technique method applies internal patterns without introducing physical particles to the polymer specimen hence preventing significant changes to the mechanical properties of the material. The feasibility of the internal fluorescent pattern for DIC measurement was established and quantified through a sequence of assessments including noise-floor, rigid body motion, and uniaxial tension tests. The working principle relies on a small amount of a photoactivatable dye, spirolactam of Rhodamine B, which is covalently bound into an epoxy network and patterned through the entire sample volume. A lithographic chrome contact mask, etched with transparent semi-randomly spaced circular features, is used on top of the polymer substrate while the dye is activated with ultraviolet light. The resulting microscale fluorescent pattern, collimated through more than 400 μm of the sample thickness, can be observed using a 514 nm excitation wavelength with a confocal microscope. The assessments demonstrated that this new non-intrusive and non-disruptive method of DIC patterning can measure strain fields on sub-surface planes in a transparent polymer matrix without bias from material deformation above that plane. To the best of our knowledge, this is the first demonstration of performing DIC using sub-surface or internal patterns without adding physical particles internally and opens the possibility of tracking material deformation in three dimensions without using the internal structure or adding particles.

Keywords DIC · Speckle techniques · Microscale · Polymers · Materials science · Internal deformation

Introduction

Polymer matrix composites have been used in structures and components for many applications. For example, the aerospace and automotive industries have been extensively using reinforced composites for light-weighting, and for high strength and stiffness [1, 2]. There is still a growing effort to replace conventional metal alloys with high specific strength polymer composites (e.g.: thermosets or temperature resistant and high-strength thermoplastics) [1, 3–5]. Recently, the infrastructure industry has also begun to use polymer composite rebar to exploit the high strength and corrosion resistance properties [6].

Composite mechanical structures in these applications undergo degradation or ageing due to environmental effects and normal operational loads. Hence, they become susceptible to fatigue cracks, impact damage and corrosion [7]. Consequently, it is important to obtain precise mechanical properties of materials and monitor deformation and strain of these structures to prevent material failures. There are

✉ M. A. Iadicola
mark.iadicola@nist.gov

✉ J. W. Woodcock
jeremiah.woodcock@nist.gov

1 Materials Science and Engineering Division, National Institute of Standards and Technology, Gaithersburg, MD, USA

2 Present Address: Materials Engineering Branch, NASA Goddard Space Flight Center, Greenbelt, MD, USA

3 Materials Measurement Science Division, National Institute of Standards and Technology, Gaithersburg, MD, USA

4 Present Address: AAAS Science and Technology Policy Fellow at Materials Sciences and Engineering Division, DOE Basic Energy Sciences, Germantown, MD, USA

5 Present Address: Lamtec Corporation, Mount Bethel, PA, USA

Published online: 01 February 2023

numerous techniques for measuring surface deformation and strain using both contact techniques (e.g.: strain gages and contact-type extensometer) and non-contact techniques (e.g.: Moiré interferometry [8], holography [9], electronic speckle pattern interferometry [10], and digital image correlation or DIC [11]).

Macroscale testing and characterization can provide material bulk properties and performance, but many deformation mechanisms occurring at the microscale level cannot be evaluated with only macroscale testing [12, 13]. For example, dissimilar material joining techniques, such as adhesive joining [14], can locally alter microstructure and mechanical properties, which can introduce unique deformation mechanisms different from those of bulk properties [15]. Therefore, it is also important to be able to characterize polymer composites locally at interfaces and to investigate local properties within the material volume.

High-resolution imaging techniques are powerful tools used to acquire measurements at various scales. Conventional *in-situ* deformation and microstructure studies are usually performed in a 2-dimensional (2D) manner and may include physical particles in the polymer substrate [12]. The measurement is done by imaging the surface or a patterned cross-section of the sample while subjecting it to mechanical loading; this does not properly capture internal deformation, since the surface deformation is not necessarily indicative of the internal deformation, and the latter is changed due to the addition of the patterning particles. Therefore, it is necessary to establish new methods to identify the mechanical properties of polymer matrix composites that correlate at different length scales (e.g., microscale, mesoscale, and macroscale). Experiments such as micro- or nanoindentation have been used to measure hardness and mechanical properties; however, indentation techniques are primarily used for surface structure studies and sometimes assume that the substrate is a stress-free single-phase homogeneous continuum [16]. Other measurement practices, such as atomic force or scanning tunneling microscopy (AFM or STM) and near field scanning optical microscopy (NFSOM), are full-field methods, but they require placing a tip on or very close to the surface of the sample. Consequently, real-time visualization capability is limited by the scan rate. Although electron microscopy methods, such as STEM (scanning transmission electron microscopy) and micro-X-ray computed tomography (μXCT) can provide internal information, they also have similar limitations [15].

DIC is an effective non-contact optical method used to measure displacements and strains on the surface [17] or within the volume of a deforming material [12]. In 2D-DIC, the intensity patterns in a subset of two images are correlated to track the subset displacement between the images. The subsets are assessed as a grid of measurement points (spaced at a user selected step size), creating a displacement field that can be used to calculate the strain values over the grid of points. When the material does not possess an inherent pattern sufficient for correlation, artificial random speckle patterns are produced on the surface of the material or by adding physical particles within the material's volume. However, the latter can alter the bulk mechanical properties of a polymer material. For example, Mohsen and Zare have investigated the effect of increasing the volume fraction interphase with nano and micro-sized particles on the mechanical properties of polymer composites [18, 19].

In a three-dimensional (3D) volume, Croom et al. in [15] used volumetric digital image correlation coupled with μXCT to probe 3D deformation behavior in carbon reinforced polymer composites in joint-affected zones to understand 3D microscale deformations in composites. Chopped carbon fiber reinforcement was used as speckles for contrasting purposes. Using the fiber reinforcement as a pattern degrades the spatial resolution of the measurement and limits its localized measurement at the interphase. Similarly, the interphase was not captured in [20], where scanning laser confocal microscopy was used to image fluorescent particles dispersed in an agarose gel. In this case, the entire volume was imaged and used for digital volume correlation.

Optical microscopy and DIC have been coupled to obtain microscale full-field surface displacement measurements. Microscale strain maps of a deforming fiber reinforced composite were investigated using DIC [21]. Due to a lack of suitable textures in the natural state of the material, the authors used a pattern produced through powder deposition on the specimen surface. Previously, Berfield et al. [12] discussed the application of DIC for full-field real-time measurements both at the micro and the nanoscale, performed on either the patterned surface or an interior plane (for transparent media) of a deforming body. A confocal optical microscope was used as the imaging device, thus considerably simplifying the experimental set-up. However, for the nanoscale internal layer, fluorescent nanoparticle tracers were physically introduced in the sample and employed for DIC measurements. This patterning technique alters the mechanical properties of the material of interest.

For this work, a non-intrusive and non-disruptive internal fluorescent pattern is designed, developed, and tested using DIC to measure internal deformation at microscale levels in an epoxy thermoset. The working principle relies on a concentration (i.e., 0.05 % of final mass of epoxy) of a photoactivatable dye, Rhodamine B spirolactam, which is covalently bound into an epoxy network and is fully dispersed through the entire sample volume without altering the mechanical properties of the material. A lithographic chrome mask, etched with transparent semi-randomly spaced circular features, is used as a contact mask on top of the polymer substrate with ultraviolet light to activate the internal fluorescent pattern. The resulting microscale

internal fluorescent pattern is activated as columns through more than 400 μm of the sample thickness and can be imaged with an excitation wavelength of 514 nm using a fluorescent confocal microscope with a 1.6 mm × 1.6 mm field of view (FOV).

The purpose of this study is to determine if the internal fluorescent pattern can be used to quantitatively measure the displacements and deformation occurring within a transparent polymer matrix when subjected to axial tensile loading. The feasibility of the internal fluorescent pattern for DIC measurement is evaluated and quantified through a sequence of assessments including noise-floor, rigid body motion, and uniaxial tension tests. Three different types of tensile test assessments are made (1) comparing mechanical properties with and without the addition of the pattern dye, (2) measurements of two internal planes on two specimens that are sandwiched together where the one specimen is loaded in tension and the other specimen is undeformed (no load or translation) to simultaneously identify the internal pattern in each specimen, and (3) comparing tensile test results for the same material being measured with the internal DIC and the traditional surface DIC. Additionally, a study is made of the DIC calibration variation with depth and experimental setup to determine the stability of calibrations of internal planes.

Materials

One composition of epoxy matrix system for thermoset polymer composites was used. It includes diglycidyl ether of bisphenol-A epoxy resin, also known as DGEBA (Epon Resin 828 purchased from Sigma-Aldrich), a curing agent, polyetheramine JEFFAMINE D-230, a difunctional primary amine purchased from Sigma-Aldrich, and a Palm dye rhodamine B spirolactam, synthesized according to published procedures by Seethamraju et al. [22]. Additional processing and curing information are found in the supplementary material (S.M.) document.

Fluorescent Molecular Patterning Dye

In the design of this potential patterning technique, fluorogenic probes with properties responding to changes in their environment, and that can transition from a dark state (off) to an emitting state (on), are of interest. One such class of molecular probes change their spectral (absorbance and/or emission) properties in response to illumination with ultraviolet (UV) light and are termed fluorophores. A specific example of a responsive fluorophore is the rhodamine spirolactam (RS) derivative shown in Fig. 1.

RS was previously employed as a UV activated fluorophore for super resolution microscopy and later as a water sensor [22]. In this work, RS is used as a photo-imageable fluorescent dye for creating a 3D internal fluorescent pattern for measurement of displacements and strains using DIC.

Sample Preparation

DIC Pattern Design and Chrome Contact Mask

A contact mask was designed with circular transparent features for the purpose of photoactivating fluorescent cylindrical regions onto the polymer RS-substrate via UV light exposure. With the mask in place over the sample, the sample was irradiated, activated, through its thickness to generate viewable and spatially accurate pattern features onto the internal planes. The lithographic pattern was generated using the Nanolithography Toolbox software package [23] developed at the National Institute of Standards and Technology. The circle radius was held at 10 μm and pattern generation proceeded by random circle placement, constrained by a minimum edge-to-edge distance of 2 μm imposed between neighboring features, which yielded an average aerial coverage of the transparent circles of 28.5%. This pattern density is within the recommended aerial coverage range of 20% to 40% for DIC patterns of circular features [24]. The purpose of this pattern design was to allow the initial assessment for use as an internal DIC pattern and was not optimized for a

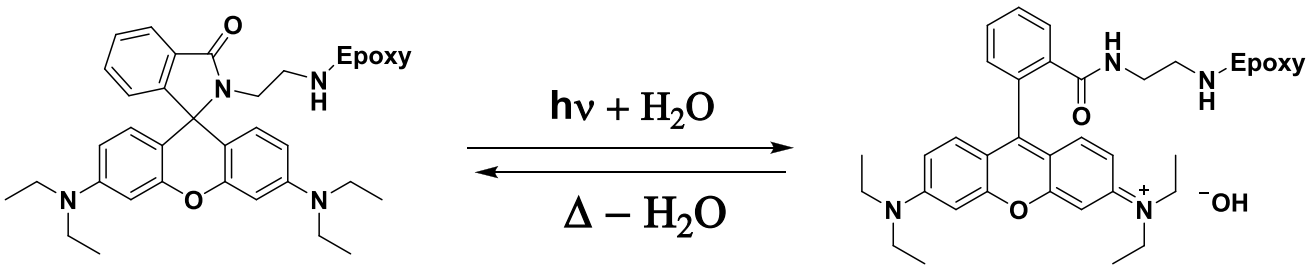

Fig. 1 Proposed activation mechanism for the ring opening of the spirolactam through applied energy and in the presence of water. Non-fluorescent or ring closed (left) and fluorescent or ring opened (right)

particular FOV. Further, optimization of the pattern feature size and spacing for a specific FOV is left for future work. Additional pattern design and specimen geometry information are discussed in the S.M. document.

Pattern UV Photoactivation

To attain an optimal activation of the pattern with minimal divergence, the contact mask and the surface of the polymer substrate need to be in direct contact. UV photoactivation was carried out on a MA8 Mask Aligner (SUSS MicroTec). The uniaxial tensile specimens with nominal gauge area 25.4 mm by 1.88 mm (cured as a kit of seven specimens as shown in the S.M. Fig. S2(b)) were placed on top of a 10 cm (diameter) silicon carrier wafer to provide mechanical support, pressed into hard contact with the mask secured above, and exposed with the collimated output of a mercury vapor lamp (a broadband UV source with measured intensities of 6.5 mW/cm^2 at 365 nm and 12.5 mW/cm^2 at 405 nm). The support wafers were coated with an AZ BARLi anti-reflective layer (Integrated Micro Materials) to suppress secondary exposure of the specimen underside due to reflections. The exposure time could then be varied to control the exposure dose; a large exposure dose increases the penetration depth of the photoactivated pattern, but risks overexposure at the specimen surface, blurring the feature edges. For the specimens (nominally 0.5 mm thick), the optimal exposure time was found to be 2000s, corresponding to an exposure dose of 13 J/cm^2 at 365 nm and 25 J/cm^2 at 405 nm.

UV exposure transfers the randomly distributed circle pattern of the photolithography mask into a corresponding pattern of photoactivated columns through the thickness of the specimen. The columns remain well defined through a depth of 400 μm, with no evidence of broadening at increasing depth due to angular divergence of the UV light source. The internal fluorescent pattern is shown in Fig. 2 using a confocal Leica microscope DM6000CS with a single charged-coupled device (CCD) microscope camera Leica DFC365 and a 10× magnification with a 1.0 numerical aperture (NA) objective. Additional internal fluorescent pattern images are illustrated in the S.M. document in Fig. S3.

Experimental Procedures

In this section we describe first the equipment used for the imaging followed by a description of the test procedures for the DIC calibration study, rigid body motion test, and various tensile experiments. The results of each of these are presented individually in the Results section. Details regarding the mechanical testing frame, DIC parameter study, and noise-floor tests are discussed in the S.M. document with only summary results shown in the Results section.

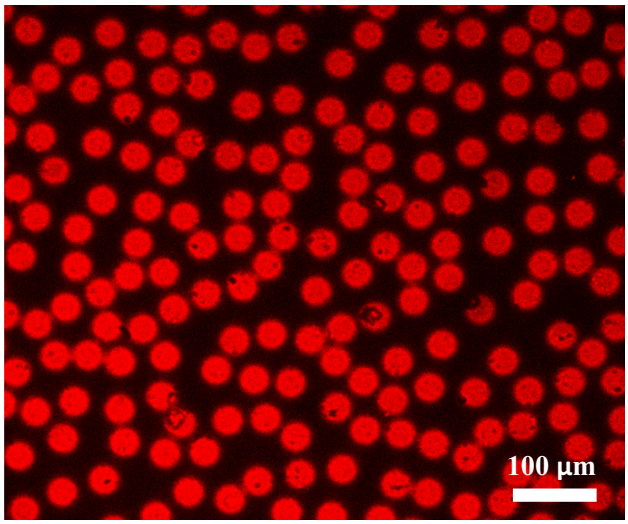

Fig. 2 False color image of the photoactivated fluorescent pattern at 10× magnification

Equipment: Microscopes

Samples with microscale internal patterns were imaged using the confocal Leica microscope DM6000CS described in Table 1. Illumination of the internal layers of the specimen was performed through excitation of the fluorescent pattern using a 514 nm laser scanning from left to right and indexing down subsequent rows of the final image. The image size of 1024 pixels × 1024 pixels and the image magnification of 1.5 μm /pixel (0.0015 mm/px) produced a total FOV of 1551.5 μm × 1551.5 μm (1.6 mm × 1.6 mm) and a depth of focus of 0.3 μm. Using this method, the major contribution to each image exposure is the internal layer of the specimen within the depth of focus while minimizing the contribution from the layers above and below. An optimum pattern size would be between 2.3 μm and 3.8 μm radius, considering the optimum pattern feature size between 3 to 5 pixels. However, for the purpose of verifying the feasibility of this new technique, a circular feature size of 10 μm in radius was selected. This pattern size results in a degradation of the DIC spatial resolution from what is possible based solely on the image resolution. A follow-on investigation to optimize the DIC pattern size is in development.

The surface pattern (for all airbrushed specimens) was imaged using an Olympus IX71 wide-field microscope with a PixeLINK Capture OEM camera and a 4× objective. The image resolution was 2048 pixels × 1536 pixels, and the image magnification was calculated to be 0.801 μm / pixel (0.000801 mm/px), which produced a total FOV of 3103 μm × 2327 μm (3.1 mm × 2.3 mm) and a depth of focus of 8.5 μm. Single camera DIC is known to suffer from false strains due to out-of-plane motion when using fixed focal length lenses. In this case, the small depth of focus restricts

Table 1 DIC reporting summary: hardware, setup, and analysis for assessment and uniaxial tests

Hardware	Leica DM6000CS Fluorescent Microscope	Olympus IX71 Wide-Field Microscope
Camera	CCD microscope camera | Leica DFC365 FX	PixelLINK Capture OEM | PL-E423CU
Camera Interface	FireWire-B	USB 2.0
Objective	10x	4x
Lighting	Scanning laser (emission wavelength of 514 nm)	Microscope stage LED
Fan	None	
Numerical Aperture	1.0	0.3
Image Resolution	1024 pixels × 1024 pixels	2048 pixels × 1536 pixels
Field of View (FOV)	1551.5 μm × 1551.5 μm (1.6 mm × 1.6 mm)	3103 μm × 2327 μm (3.1 mm × 2.3 mm)
Information Depth (Depth of Focus)	0.3 μm	8.5 μm
Image Scale	667 pixels/mm	1248 pixels/mm
Exposure Time	15.4 s	1.0 s
DIC Analysis Setting		
DIC Software	Vic-2D version 6.2.0, build 1321	
Subset Size	91 pixels × 91 pixels**	
Step Size	30 pixels**	
Subset Shape Function	Affine	
Correlation Criterion	Normalized sum of squared differences (NSSD)*	
Strain Type	Hencky	
Strain-Filter Size	5**	
Image Acquisition Rate	Manual (1 image/min.)	
Patterning Technique	Internal fluorescent dye	White base paint + airbrushed speckles
Approximate Pattern Feature Size	29 μm	21 μm
Virtual Strain Gauge (VSG) size	211 pixels (0.32 mm)	211 pixels (0.17 mm)
VSG Equation	(Strain-Filter Size – 1) * Step Size + Subset Size	

*Unless otherwise specifically noted. Zero-normalized sum of square differences (ZNSSD) was applied in some cases, and this is specifically noted

**Based on initial DIC parameter study (see S.M. for details)

the possibility of measuring the specimen surface if it should move out-of-plane.

The microscope setups for the internal pattern and the surface pattern tests are summarized in Table 1, along with the key DIC analysis parameters that were used for each.

DIC Calibration

For DIC image acquisition, a single camera was used (2D-DIC), which, in combination with a microscope, may introduce complex distortions [25] requiring correction. A two-step process was used for the calibrations here. First, the image scale was assessed using a traceable graduated slide. Multiple measurements were made and averaged to reduce some of the uncertainty in the image scale determination. Second, an inverse mapping process was used to correct the complex distortions present in the microscope imaging setup [26–28]. This results in the determination of a 10 × 10 grid of spline coefficients covering the image that maps from the distorted pixel space to the undistorted and includes both the image scaling and the non-linear distortions. The distortion correction procedure requires images of a patterned object, as it is translated to a series of rigid-body motion positions in the two orthogonal planar directions. The resulting distortion correction is only valid for a specific aperture, focus, camera geometry and zoom level, so these were fixed before the required rigid-body motion translations (and calibration image acquisition) were started. For each distortion correction, a specimen patterned as described above was used, with a total motion of approximately 15 % of the field of view and each translation step in the sequence of approximately 3.75 % of the FOV. This distortion correction procedure was used for both the surface patterned and internal fluorescent patterned specimens.

To assess the variability of the calibration at various planes within the depth of the specimen, a series of calibrations were performed on a single specimen near the surface and eight additional positions within the depth of the specimen (shown schematically in Fig. 3). The image scale was set based on the traceable graduated slide and assumed to be unchanged through the change in depth. This assumption will be assessed during the rigid body motion test. A single

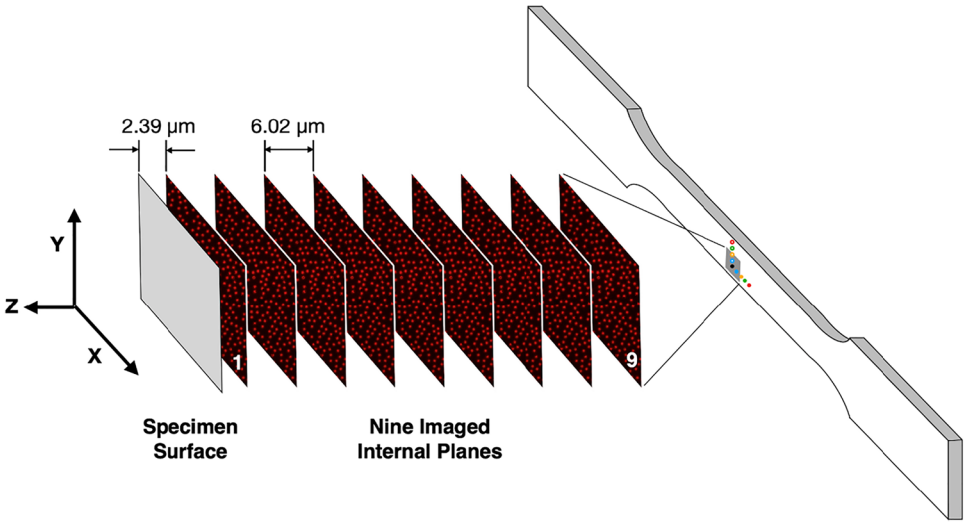

Fig. 3 Schematic of the uniaxial tensile specimen calibration *X* and *Y* displacement shifts (color points, see Fig. 8a) and close-up of nine imaged planes within the depth of the specimen

specimen was securely affixed on a glass slide, which was mounted on top of the microscope piezoelectric positioning stage. Focus checks and uniform intensity were used to ensure that the motions in the *X*-axis and *Y*-axis were in the exact plane of the pattern itself. Near the surface of the sample (plane 1 in Fig. 3) and at the 8 additional internal planes (in the *Z*-direction), a reference image was taken; then images at each of the required rigid-body motion translations (color points in Fig. 3) were also captured. Each step in the *Z*-direction (through the thickness of the sample) was captured at every 6.02 µm, which was greater than the 4.77 µm *Z*-resolution (that is the depth of field) of the microscope imaging, making each measurement independent of the others. The applied translations were from approximately 50 µm to 290 µm with a return to zero in the *X*-direction and from approximately 50 µm to 230 µm in the *Y*-direction with a return to zero. These same images are used for the rigid body motion tests below.

Rigid-Body Motion Test

A rigid-body motion test, or extended noise-floor test, is typically used to assess the systematic bias and uncertainty due to uncorrected lens distortions [25]. Whereas the basic noise-floor test is applied with almost no motion. The extended noise-floor or rigid body motion test has substantial motion, however still with no deformation of the specimen. The same rigid-body translation images used to investigate the variation in calibration with depth (as described above in *DIC Calibration*) were also used to verify the ability of DIC to measure displacements at the 9 planes (spaced at 6.02 µm increments) into the depth of the specimen. The applied translations were from nominally 50 µm to 290 µm with a return to zero in the *X*-direction and from nominally 50 µm to 230 µm in the *Y*-direction with a return to zero. At each position, the images were taken at all 9 internal planes. That is, the measurements at each depth were made sequentially during the individual position holds, so one would not expect any changes in the (*X*, *Y*) positions with depth at any one hold location. This fact will allow assessment of the assumption that the image scale did not change with depth, in that the position would change systematically with depth if there was an appreciable image scale change. The repeatability of the microscope positioning stage motions was not sufficient to exactly know the applied translations, thus a comparison of the displacements to known positions will not be possible.

Tensile Experiments:

1) *Comparison of Material with and without Pattern Dye*

This experiment measures the uniaxial stress–strain response of specimens containing the photo-imageable fluorescent dye (with the same percentage, 0.05 % of final mass of epoxy, as those used throughout this work) and specimens without the dye to determine if the addition of the dye has any effect on the resulting mechanical properties. Specimens containing no dye were exposed to the same conditions as those with dye. Three repeated tests are performed on specimens of each formulation of material. Since only one set of the specimens could have an applied internal DIC pattern, only a typical surface DIC with an airbrushed pattern was used for consistency. The tests are performed using a compact tensile frame (Fig. S4 in the S.M.) and imaged using the wide-field microscope (Table 1). Only the bulk properties are considered here.

2) *In-Plane Tension above a Rigid Body Specimen (Sandwiched Specimens)*

This experiment measures two internal planes: one on each of two specimens that are sandwiched together on the tensile frame where the top specimen is loaded in tension and the bottom/lower specimen is undeformed (no load or translation). Each specimen is separately patterned. The testing setup diagram appears in Fig. 4. Unfortunately, perfect contact between the two specimens could not be achieved, so the internal fluorescent pattern in the bottom specimen was imaged through multiple refractive indices: air, the entire top specimen, another layer of air (between the sandwiched specimen), and through a portion of the bottom specimen. Only the top specimen (#4) was clamped on both ends while the bottom/lower specimen (#3) was only gripped on one end and cut on the other. The cut end of Specimen #3 was free. Another experiment where the specimen that is being deformed in tension is below the specimen that is not deformed is described in the S.M. document as *Additional Tensile Experiment*: *In-Plane Tension below a Rigid Body Specimen*.

The tensile frame is positioned, so the 1551.5 µm × 1551.5 µm FOV is within the specimen's length (i.e., 25.4 mm) of the reduced width section. The total nominal thickness of the sandwiched specimens is 1.0 mm. The grip displacement loading is applied in steps (as described in the *Equipment: Testing Frame* section of the S.M.), and after each step, a one-minute pause in loading was performed before the next loading step.

A pair of images (one in each specimen, see Fig. 4) was captured at the end of each pause prior to the next loading step. The procedure was repeated until the specimen (#4) under tension broke. The specimen (#3) underneath did not undergo any applied translation or deformation.

To measure the strain in the patterned top specimen (#4), the microscope piezoelectric positioning stage was translated in the *Z*-direction until the focal plane was focused on an internal plane, 350 µm below the surface of the specimen. The 514 nm wavelength laser was rasterized to illuminate the pattern and create the reference image. Subsequently, a reference fluorescent image was also captured 40 µm below the top surface of the bottom specimen (#3). This process was repeated at each step after the end of each pause until failure occurred in Specimen #4. Each image was analyzed using the Vic2D Correlated Solutions software. For all the images of the internal fluorescent pattern, the background was black, and the circular fluorescent features appeared white upon excitation when viewed with the black and white camera.

3) *In-Plane Tension Comparing Internal to Traditional DIC*

Additional tensile tests were conducted on the tensile frame, each with a single specimen under load to compare the internal DIC measured strains (Specimen #6) to surface DIC measured strains (Specimen #7). Specimen #6, already photoactivated with the internal fluorescent pattern and loaded in tension, was imaged using the fluorescent microscope (Table 1) with the same 10 × magnification. The strain was measured in the specimen similarly to the previous tensile experiments. The microscope piezoelectric stage was positioned, so the reference fluorescent image was scanned approximately 40 µm below the surface of the specimen. For each strain step, an image of the entire FOV was acquired of the specimen's internal plane, after the strain step and the one-minute hold time.

Specimen #7, with traditional microscale surface DIC pattern, was also tested. The surface pattern was generated

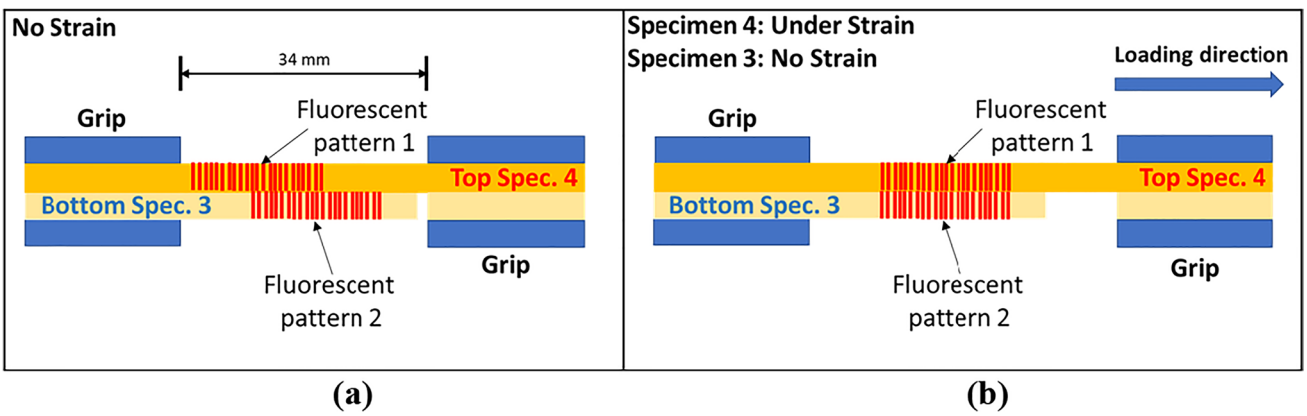

Fig. 4 Diagram of sandwiched specimens (**a**) Specimen #4 is gripped on both ends and Specimen #3 is only gripped on one end and free on the other; (**b**) Specimen #4 is solely pulled in tension on the frame

by applying matte-white base paint and a matte-black airbrushed speckle overspray on the area within the reduced width section of the specimen. The DIC calibration for the wide-field microscope (Table 1) used for this specimen was performed using the same procedure described above, except that it was only necessary for the surface Z position. For Specimen #7, the same concentration (i.e., 0.05 % of final mass of epoxy) of fluorescent dye (inactive) was incorporated into the polymer matrix. The experiment was consistent with the previous ones with photoactivated internal fluorescent patterned samples. A reference image of the entire FOV was captured before loading the specimen. The next image was taken after the first grip displacement step and hold. The imaging procedure was repeated during step loading until failure of the specimen.

Results

In this section we describe the results of the DIC calibration study, noise-floor tests, rigid body motion test, and various tensile experiments whose procedures were described previously in the Experimental Procedures section.

An initial DIC parameter study, described in the S.M. document, was used to determine the parameters that are used for all the DIC analyses in the remainder of this work, as shown in Table 1. It should be noted that a similar study could be performed for the surface airbrushed pattern, which could result in a different set of parameters; however, for simplicity, the one set is used for both the surface and internal patterns.

DIC Calibration

Calibration of the DIC imaging system is critical for a good DIC measurement and determines the image scale and distortion corrections [24]. In this work, a vendor specific method is used to correct the complex lens distortions that occur in optical microscopes [26]. Application of this method internally to multiple planes is new; therefore, a detailed assessment of the results is presented here. Independent calibrations were determined at each of the nine planes within the depth. As described earlier, each calibration is a combination of the linear component (i.e., image scaling) and a non-linear distortion correction applied using spline coefficients. The same image scale was applied to all the calibrations based on measurement of images of a traceable graduated slide. The assumption that this is true for the internal layers is verified below (see *Rigid Body Motion Test* results). The non-linear component of the calibration can be visualized by first subtracting the linear component based on the applied image scale. In Fig. 5(a) and (b), the remaining non-linear distortion is plotted for the X-direction and Y-direction, respectively, for the first layer just below the surface of the specimen (2.39 μm as shown in Fig. 3). The distortion in the X-direction is a combination of a radial variation and a single oscillation from left to right in the image, while the Y-direction distortion is predominantly a single oscillation from top to bottom in the image. These seem to be a barrel distortion in the X-direction and a drift-like distortion (like Sutton and Kammers [29, 30] showed for scanning electron microscope, SEM, images) in the Y-direction. The drift-like distortion observed in our work is a spatial effect from the laser raster path (row scan followed by step in column), which is similar in structure to the drift distortion seen in an SEM. However, in the case of the laser drift-like distortion, it occurs during the exposure time of a single image and is not continual over the time of the experiment.

Since the raster of the laser illumination is along the X-direction then stepped in the Y-direction, it is believed that the drift-like distortion is predominantly the result of the laser raster accuracy. Figures 5(c) and (d) are the equivalent plots for the fifth layer (26.47 μm) into the depth, while Fig. 5(e) and (f) are for the nineth layer (50.55 μm) into the depth, at the same color scale range for each direction. Qualitatively, the non-linear distortions are quite similar over all nine layers within the depth. For demonstration purposes, only the top, middle, and deepest layers are shown, however the remainder are shown in the S.M. To show the relative difference field, the non-linear distortion of the near-surface layer is subtracted from the fifth and nineth layers and are plotted in Fig. 6, at the same color scale range for each direction. The differences are half the magnitude in the Y-direction and about a tenth the magnitude in the X-direction as compared to the total non-linear distortion (Fig. 5). These minimal differences suggest the majority of the distortion correction can be captured with the near-surface layer calibration and potentially used for all the layers within the depth of the specimen. The same images used for the calibrations are used for the *Rigid Body Motion Test* analysis. Although the calibrations were performed only over the first 50.55 μm of depth, the fluorescent pattern was confirmed to be visible through about 400 μm of specimen depth.

During this investigation, some anomalies led to questions regarding the calibrations. It was determined that when using the tensile frame on top of the microscope positioning stage, the positioning stage oscillated to maintain the tensile frame's position. Apparently, the microscope positioning stage could not sustain a fixed position, due to the weight of the tensile frame and was constantly moving slightly to correct its position. Figure 7(a) and (b) shows the non-linear distortion for the X and Y directions, respectively, determined for a layer at 40 μm depth while using the tensile frame, and Fig. 7(c) and (d) shows the differences of this calibration from the one without the tensile frame (Fig. 5(a) and (b)). The color scale ranges in each direction are the

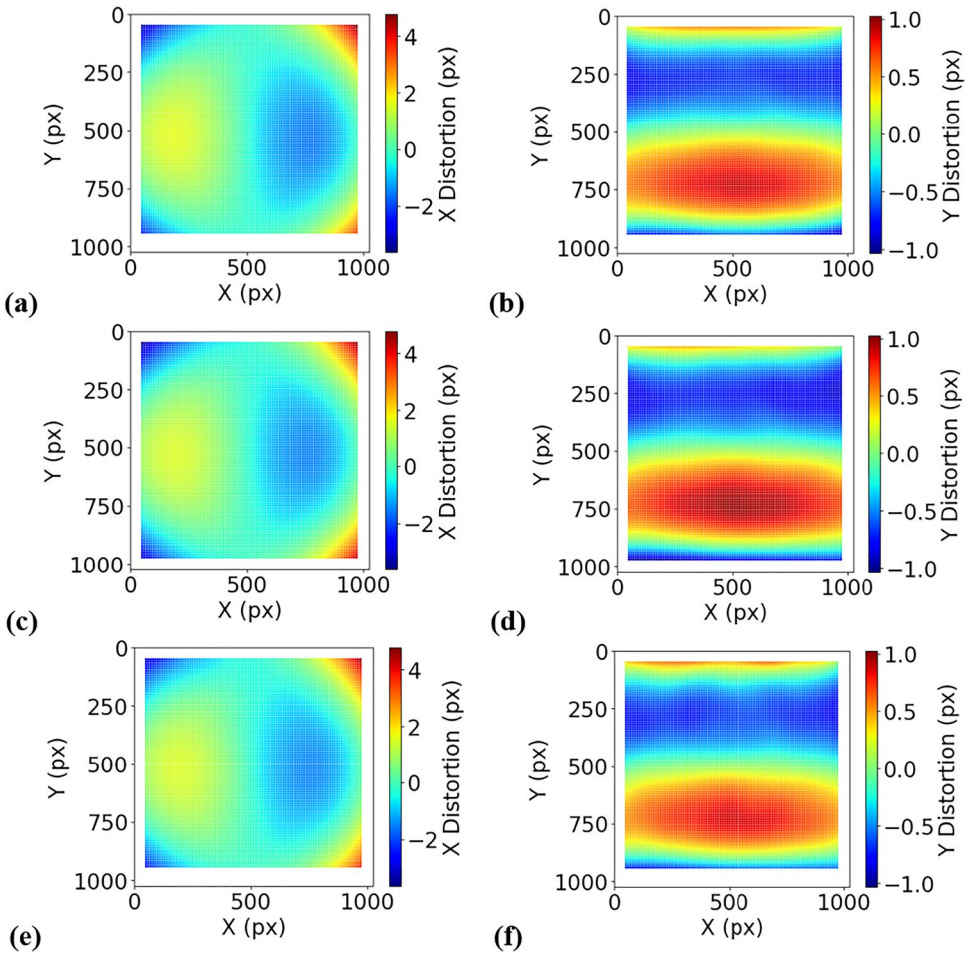

Fig. 5 Non-linear distortion correction in pixel in the *X*-direction (**a**), (**c**), and (**e**), and in the *Y*-direction (**b**), (**d**), and (**f**) for calibration on first (**a**-**b**), fifth (**c**-**d**), and nineth (**e**–**f**) layer into the depth (see Fig. 3)

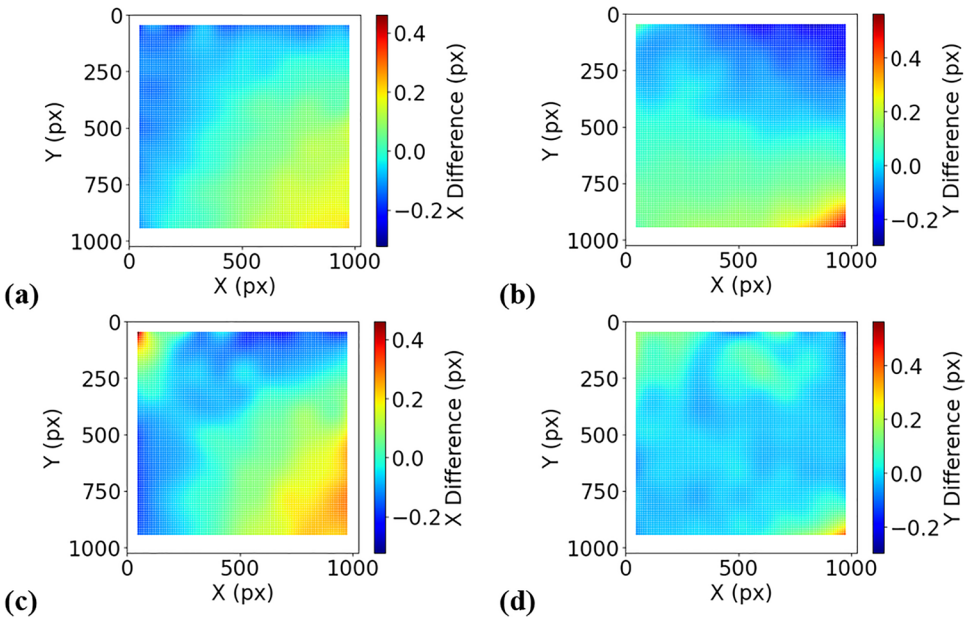

Fig. 6 Difference plots of the non-linear distortion correction in pixel in the *X*-direction (**a**) and (**c**), and in the *Y*-direction (**b**) and (**d**) for calibration fifth layer (**a**-**b**), and nineth layer (**c**-**d**) into the depth after subtracting the first layer distortion. For example, for the *X*-direction (**a**) is Fig. 5(c) minus Fig. 5(a), while (c) is Fig. 5(e) minus Fig. 5(a)

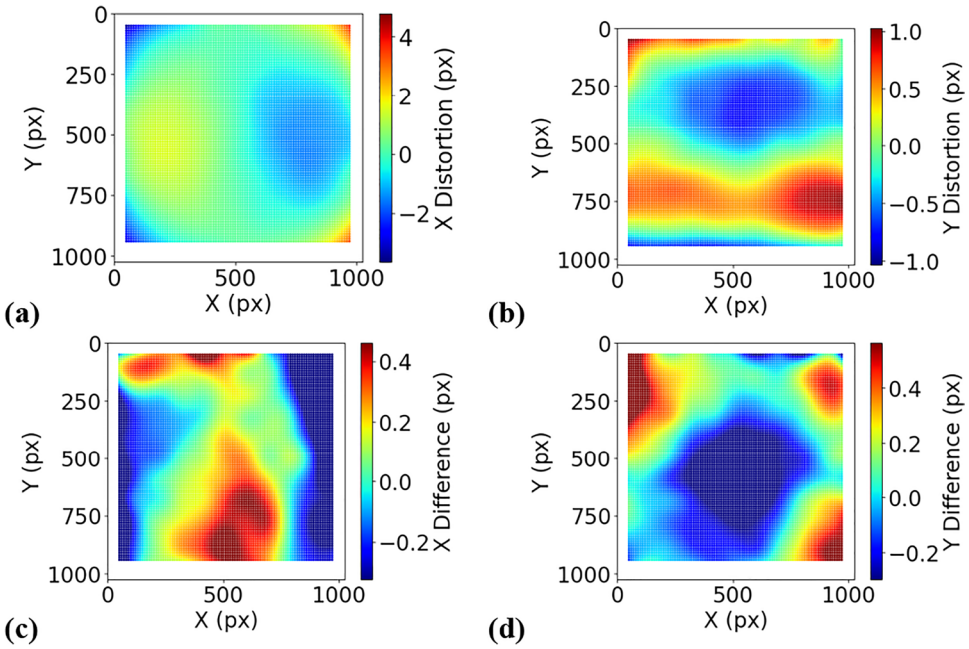

Fig. 7 Non-linear distortion correction for specimen in the tensile frame in pixel (**a**) in the *X*-direction and (**b**) in the *Y*-direction, and difference plot of the non-linear distortion correction in pixel (**c**) in the *X*-direction and (**d**) in the *Y*-direction for calibration with the tensile frame subtracting the first layer distortion correction without the frame (Fig. 5(a) and (b) similar to the Fig. 6)

same as used in Figs. 5 and 6 for the distortion and the differences. Although the overall structure of the distortion (Fig. 7(a) and (b)) is similar, the features are smoothed out in the case of the tensile frame. This results in a calibration that does not fully correct the distortions when using the tensile frame, but also suggests that when the microscope positioning stage is holding the tensile frame, there will be some added uncertainty in measurements even when using the superior calibration (i.e., the near-surface layer calibration performed without the tensile frame, see the noise-floor results below). For example, this would be the case during the tensile experiments shown below.

Noise-Floor Test

Table 2 summarizes the results for e_{xx} and e_{yy} at nominally 40 μm depth for the spatial noise-floor and rigid body motion noise-floor [24] performed without the tensile frame, and the spatial, rigid body motion, and temporal noise-floors with the tensile stage. For each case, the results are shown for analysis using the layer specific calibration and the near surface layer calibration (Fig. 5(a) and (b)). In the remainder of this paper, unless otherwise noted, the calibration for the first layer within the depth and without the tensile frame is used for all the other depths, since it was shown that the majority of the distortion correction can be captured well by the near-surface layer calibration without the added noise of the tensile frame and positioning stage issues. This is the case for all *Tensile Experiments*, which use the near-surface calibration without the tensile frame even for tests performed with the tensile frame.

In Table 2, there is no substantial difference in the noise floor using the near surface calibration versus the layer specific for any of these assessments. Using the tensile frame increased the noise-floor by almost a factor of three from the static noise floor due to the positioning stage motion, whereas the rigid body motion (without the tensile frame) only increased the noise floor by about 50 % on average. There was little to no difference seen between the temporal and spatial noise floors when the tensile frame was used. Overall, the mean strain in the e_{xx} is smaller than in the e_{yy}, and that the e_{yy} is always more negative than the e_{xx}. It is suspected that this might be related to the laser raster in the *Y*-direction. When using the tensile frame, the uncertainty in strain due to the motion of the microscope positioning stage dominates any additional uncertainty due to a calibration using the tensile frame along with the microscope positioning stage.

Rigid-Body Motion Test

Recall that the rigid-body motion test, or extended noise-floor test, is typically used to assess the systematic bias and uncertainty due to uncorrected lens distortions [24]. Here the same rigid-body translation images used to investigate the variation in calibration with depth (as described above in *DIC Calibration*) were also used to verify the ability of DIC to measure displacements at the 9 internal planes. The specimen was held on a glass slide (the tensile frame was not used), and the images were correlated using the individual layer calibrations determined above. A review of the field plots of displacements and strains showed no systematic

Table 2 Summary of noise-floor results (in μm/m) at a nominal depth of 40 μm (see S.M for analysis details)

	Layer specific calibration	Near surface layer calibration
Static Spatial Noise-Floor		
mean(exx)	24	9
stdev(exx)	289	286
mean(eyy)	-67	-66
stdev(eyy)	290	262
Rigid-Body Motion Test (Spatial Extended Noise-Floor)		
mean(exx)	2	45
stdev(exx)	378	338
mean(eyy)	-19	-19
stdev(eyy)	436	530
Tensile Frame Spatial Noise-Floor*		
mean(exx)	-26	-33
stdev(exx)	838	946
mean(eyy)	-70	-60
stdev(eyy)	813	775
Tensile Frame Rigid-Body Motion Test		
mean(exx)	171	184
stdev(exx)	2230	2370
mean(eyy)	-47	308
stdev(eyy)	1870	2482
Tensile Frame Temporal Noise-Floor**		
mean(exx)	-27	-33
stdev(exx)	760	762
mean(eyy)	-70	-60
stdev(eyy)	713	697

* based on average spatial noise 74 no motion images

** based on average of approximately 900 points tracked through 74 sequential images

structure that might indicate uncorrected lens distortions (following Sect. 3.3 of [24]). At every individual rigid-body motion displacement, Fig. 8(a), the spatial standard deviation of displacement was typically about 0.21 μm (0.14 px) for both U and V displacements (shaded regions of Fig. 8(b) and (c)); However, the variation of the spatial average displacements over the 9 planes within the depth was more substantial for both U and V displacements (line and points in Fig. 8(b) and (c) plotted on a common range of displacement). For clarity, the X and Y-displacements are shown as U and V, respectively, in Fig. 8 and the remainder of this work. These changes in the average displacement are about 3.8 and 2.4 times the individual standard deviations at the largest depth, respectively. This would suggest that there might be a change in image scale with depth, which would not be unexpected.

Plotting the total displacements, D, (combined U and V displacements) for each layer versus the displacements from the first layer as a reference, Fig. 9(a), shows that any change in the scale is quite small (i.e., the data lie on top of each other). The slope of the data for each layer was fitted using a simple linear fit and the SciPy Optimize. curve_fit function [31], which included weighting each data point based on the uncertainty of each point. The resulting slopes are plotted in Fig. 9(b) with the propagated uncertainties in the case of the SciPy function. These results suggest that there may be a small change in scale (of about 0.1 %) at the largest depth, but it is almost within the uncertainty of the slope determination. Additionally, the scaling effects shown in Fig. 9 were investigated as well for the individual displacement directions and using only the calibration from the first layer for all the layers into the depth. It was found that although there was more variation in the V slopes, the overall trend and magnitude of the slopes in the individual displacement directions were consistent with Fig. 9(b) using either calibration. Further investigation into this slight scaling difference is left to future work since our quantity of interest is strain and not the displacements, and small changes in depth will not result in large changes in scaling that might affect the strain determinations.

The bias (i.e., deviation from zero strain or strain error) and uncertainty were also analyzed for the 9 internal planes and 8 translation positions (Fig. 8(a)) and are shown in Fig. 10. The spatial standard deviation of the e_{xx} strain (shaded areas in the Fig. 10(a) and (b)) was 0.0003 mm/mm on average with a minimum of 0.0001 mm/mm and a maximum of 0.0006 mm/mm. Whereas, the spatial standard deviation of the e_{yy} strain (shaded areas in the Fig. 10(c) and (d)) was 0.0004 mm/mm on average with a minimum of 0.0001 mm/mm and a maximum of 0.0007 mm/mm. The uncertainty tended to increase with depth, and the increase was more substantial beyond 30 μm. Similar behavior was seen in the static noise floor without motion and without the tensile frame (as shown in the S.M.). It is interesting to note that the SciPy calculated slopes Fig. 9(b) seem to only increase at depths greater than 30 μm as well.

The spatial average of the strains deviated from the known zero value (assuming pure rigid-body motion, black dashed lines in Fig. 10) by a maximum of 0.0001 mm/mm in e_{xx} and 0.0003 mm/mm in e_{yy}. This larger bias in average e_{yy} than e_{xx}, as well as the more negative values of e_{yy}, are consistent with the noise-floor results in Table 2. In all cases in Fig. 10, the deviation from zero (or strain error) was within the spatial standard deviation of strain for that image, that is any bias in the strain was within the uncertainty of the strain measurement.

A similar rigid body motion test analysis could be applied to the images taken with the tensile frame used for the calibration (Fig. 7) at just the one depth used. The results of that analysis show average strain uncertainties of 0.0022 mm/mm

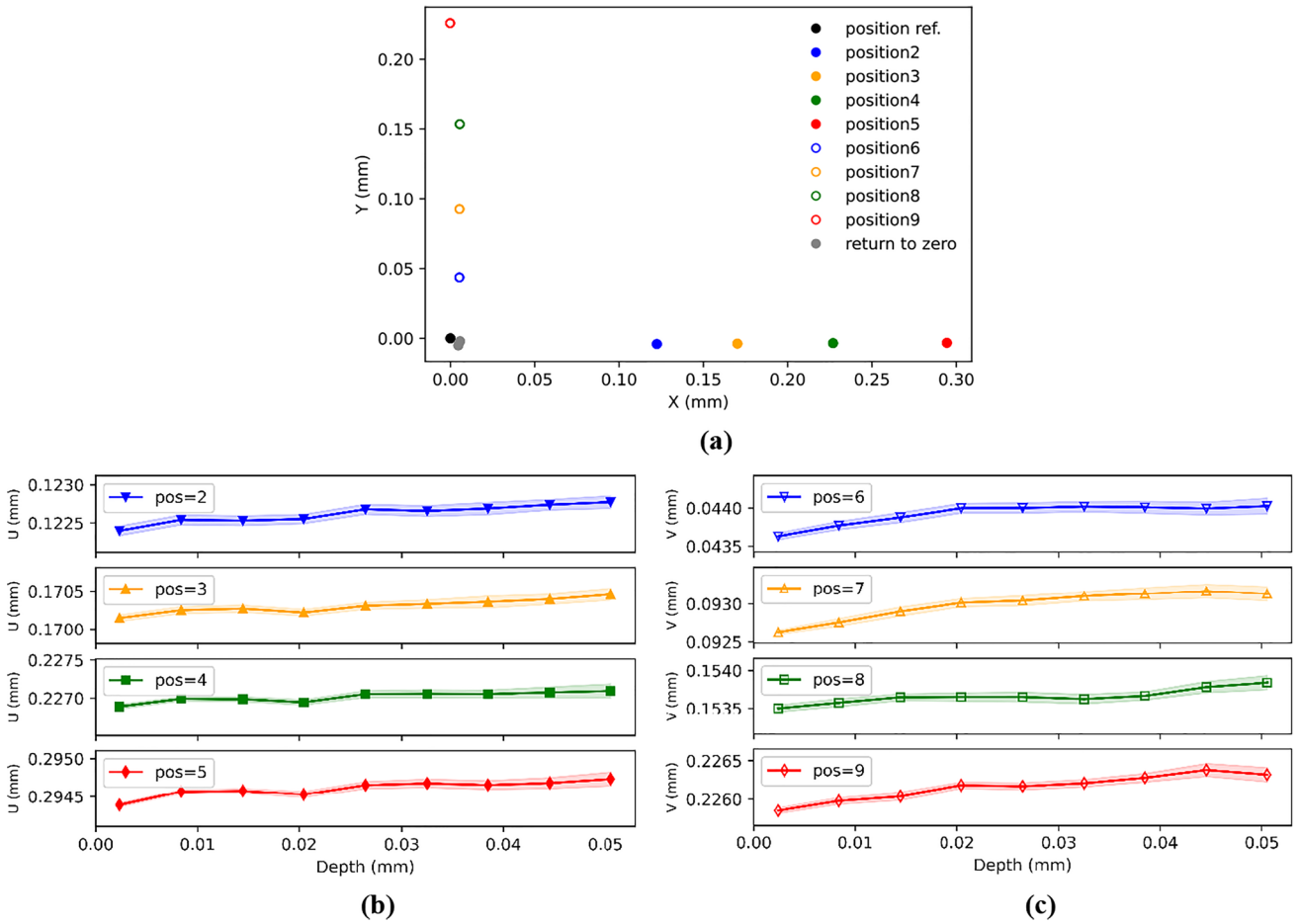

Fig. 8 Positions (**a**) from the reference position (black circle) used for U (filled circles) and V (open circles) displacements as measured by DIC (gray points are the two return to zero position, showing the lack of position repeatability). The measured position variation with depth (shading shows ± one standard deviation) for (**b**) the U and (**c**) the V displacements

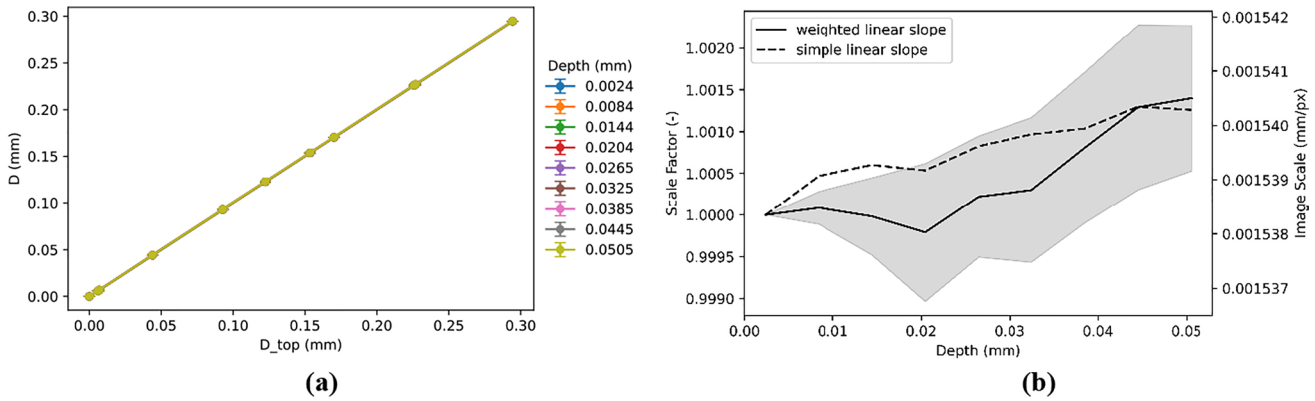

Fig. 9 **a** Total displacements, D, from Fig. 8(a) for all the points plotted vs. the top layer displacements at all nine depths (layers), and (**b**) change in fitted slopes of the data in (**a**) with depth (calculated uncertainty of slope shown as shaded area)

and 0.0019 mm/mm for e_{xx} and e_{yy}, respectively. Although these are about seven times larger in magnitude than without the tensile frame, they are not even three times larger than the noise-floor results with the frame in Table 2. Therefore, it is assumed that if the microscope positioning stage issues related to the tensile frame can be corrected in future work,

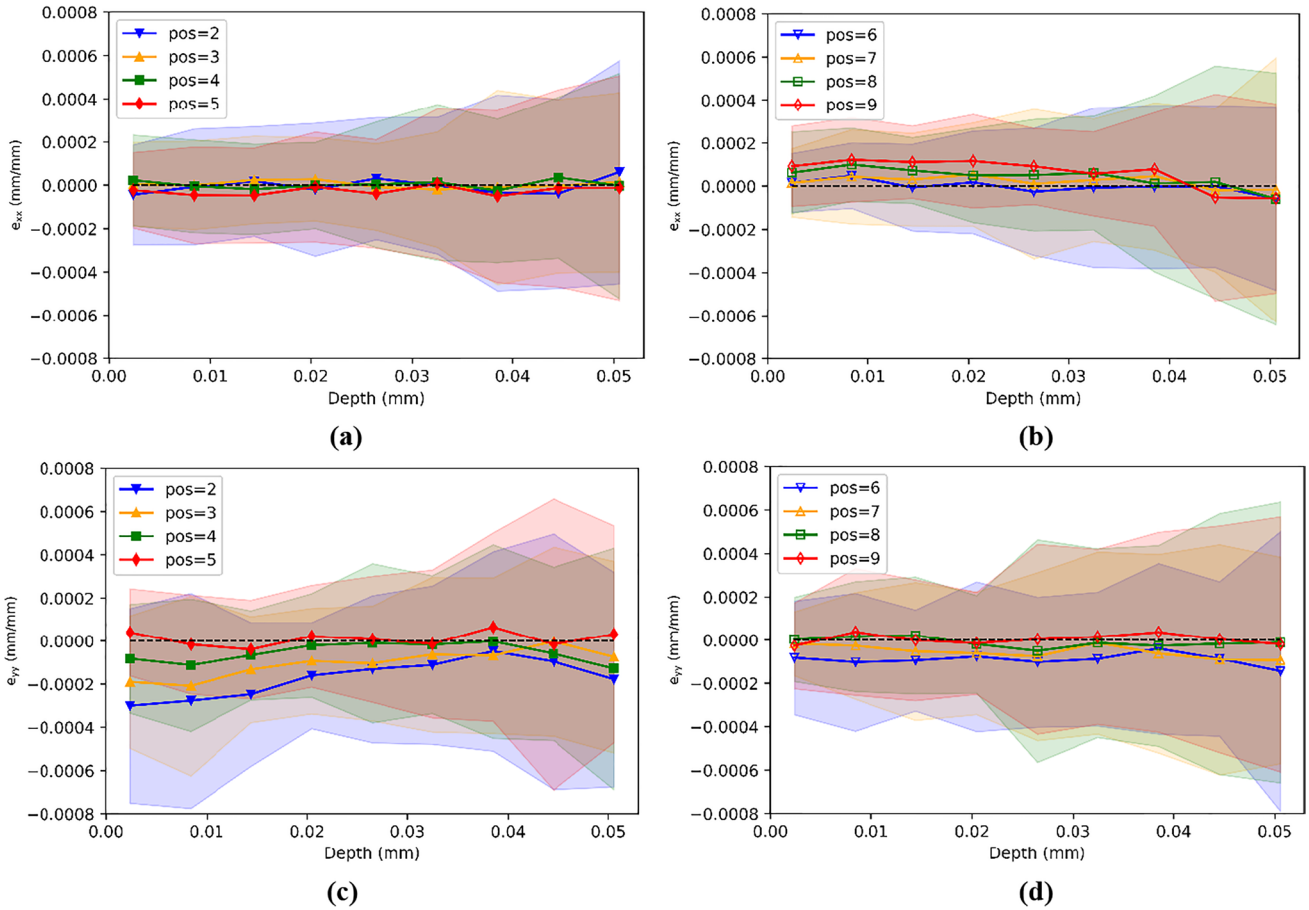

Fig. 10 Strain analysis of DIC measured true strain versus e_{xx} for (**a**) *U*-displacements and (**b**) *V*-displacements, and e_{yy} for (**c**) *U*-displacements and (**d**) *V*-displacements. Spatial average values shown as points and one standard deviation shown as shaded areas

then one could expect a reduction in both noise-floor and rigid body motion noise commensurate to the noise floor and rigid body motion noise without the tensile frame.

Tensile Experiments:

1) *Comparison of Material with and without Pattern Dye*

For *Tensile Experiment 1*, specimens with and without the photoactivated dye were tested uniaxially to determine if the dye had any effect on the macroscopic mechanical response of the material. Specimens containing no dye were exposed to the same conditions as those with dye. The modulus and maximum strength of 6 samples (3 with dye and 3 without dye) were determined from tensile experiments with airbrushed surface patterned specimens (Fig. 11). In the figure, average DIC strains (see wide-field in Table 1 for DIC details) were measured for the entire FOV during the holds. These points are shown and used in the strength and modulus determinations. The maximum strength and elastic modulus are 51.6 MPa (±4.6 MPa) and 2.9 GPa

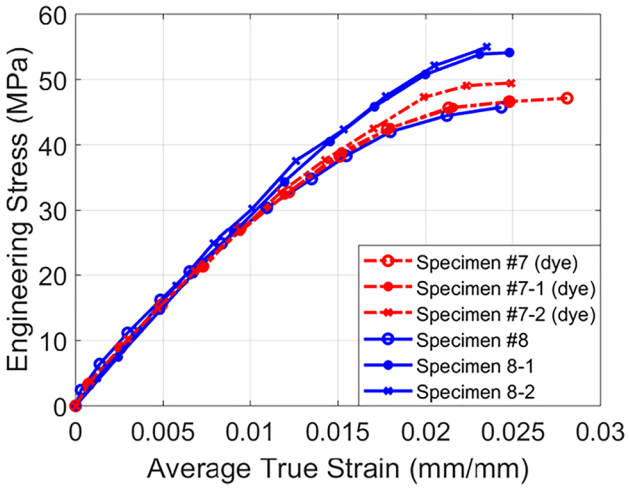

Fig. 11 Engineering stress versus true strain relationship of 6 polymer specimens (3 containing the fluorescent dye, in red dashed lines, and 3 containing no dye, in blue solid lines). All samples are conditioned at the same humidity (60 % RH)

(±0.2 GPa), respectively, for specimens without dye, and 47.7 MPa (±1.4 MPa) and 2.7 GPa (±0.1 GPa), respectively, for specimens with dye. The true strain at maximum stress for specimens with and without dye are 0.0259 mm/mm (±0.0017 mm/mm) and 0.0242 mm/mm (±0.0006 mm/mm), respectively. These results show the difference in the average values (of the strength and elastic modulus) were within one standard deviation of each other, so adding a small percentage of dye (i.e., 0.05 % of final mass of epoxy) to the polymer sample, as was done throughout this work, has no significant impact on the constitutive behavior of the polymer matrix, thus making this technique a non-intrusive method of obtaining an internal DIC pattern.

2) *In-Plane Tension above a Rigid Body Specimen (Sandwiched Specimens)*

For *Tensile Experiment 2*, the sandwiched specimens were tested, with only the top specimen under strain (Fig. 4). The results are shown in Fig. 12(a). For each hold in loading, the measured spatial average strain is shown as a data point with measured spatial ± one standard deviation of strain shown as the shaded area. The top specimen exhibits a steady increase in strain followed by a sudden decrease due to the onset of necking occurring outside of the FOV (Fig. 12(a)) with strain uncertainties averaging about 0.0017 mm/mm strain, consistent with the rigid body test noise level when using the tensile frame. The average strain in the undeformed specimen deviates from zero by as much as 0.0024 mm/mm strain, and the uncertainty is 0.0033 mm/mm strain on average, which is almost twice the rigid body test noise level when using the tensile frame. This is likely due to the number of changes in refraction index in the optical path when compared to the average uncertainties of the top specimen. The internal fluorescent pattern in the bottom specimen was imaged through air, 0.5 mm of the (top) polymer specimen, another layer of air (between the sandwiched specimens), and 40 μm of the bottom specimen. Although the lower undeforming pattern was imaged through the upper deforming pattern, there is no bias toward the tensile strains of the upper specimen seen in the average strains for the lower specimen. This would suggest that although the lower specimen did show higher uncertainty due to the multiple refractive index changes, the average strain values were not influenced by imaging through the deforming specimen. An additional experiment was performed with the position of the deforming specimen in the bottom position (details in the S.M.). The results are shown in Fig. 12(b) plotted similarly to Fig. 12(a).

In both tests, some unexplained shadows appeared in the images of the bottom specimen that locally affected the contrast. This was presumed to be the result of imaging through the upper sample and pattern. To potentially correct for these contrast changes, the use of zero-normalized sum of square differences (ZNSSD) correlation criterion was also investigated (results shown as gray dashed lines and shaded areas in Fig. 12). The use of ZNSSD had little effect on the top specimen results, but it did reduce the uncertainty of the bottom specimen (to about the rigid body test noise level when using the tensile frame) while increasing the bias at applied grip displacements between 0.8 mm and 1.0 mm. It suggests there might be an advantage (reduction of the uncertainty, but at the cost of potentially adding bias) to using the ZNSSD correlation criterion to correct for imaging irregularities, such as these, in deeper layers of a specimen. The advantage of using

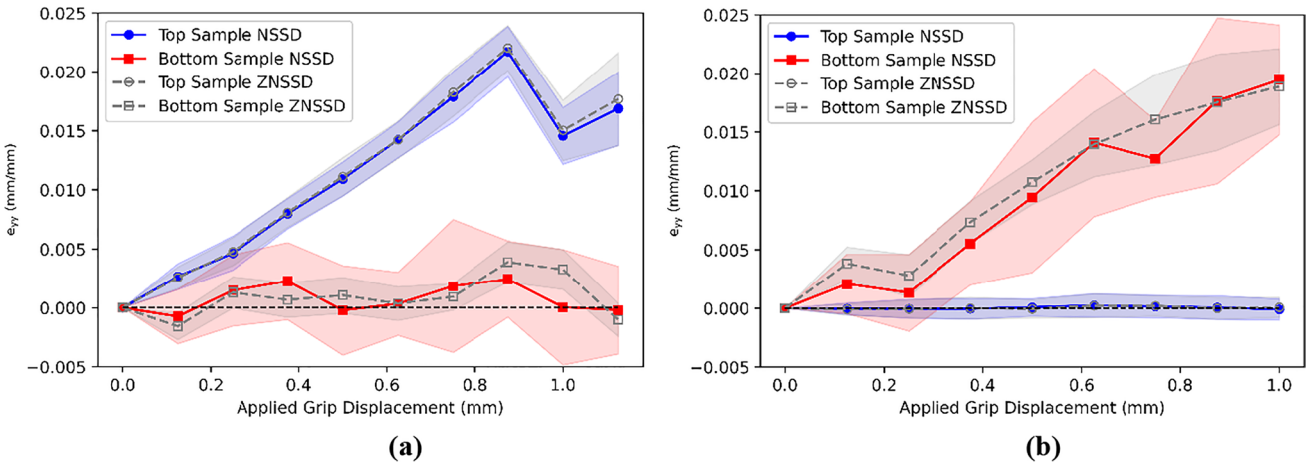

Fig. 12 DIC measured average true strain variation with applied grip displacement for sandwiched specimens. In (**a**) *Tensile Experiment 2*, the top specimen (blue circles) is strained while the bottom specimen (red squares) is unstrained. Shaded areas are ± one standard deviation, gray points and shading refer to ZNSSD correlated results for the same images, and the dashed black line is zero strain (expected value for the unstrained sample). In (**b**) are similarly plotted results for specimens in reverse position (see S.M. for details)

ZNSSD in the noise-floor and rigid body motion tests was also evaluated, and much like the Fig. 12 results for the top specimen, no advantage nor disadvantage was found. Future work should look more into potential value in using ZNSSD for this type of work. Comparing Fig. 12(a) and (b), uncertainties for the bottom specimen are similar, but uncertainties for top specimens are slightly different, probably due to an improvement in lightning condition that resulted in better contrast in the images of the pattern in the tensile experiment in Fig. 12(b).

3) *In-Plane Tension Comparing Internal to Traditional DIC*

In *Tensile Experiment 3*, an internal fluorescent patterned specimen tested in tension on the fluorescent microscope (Table 1) is compared to surface airbrushed patterned specimen tested in tension on the wide-field microscope (Table 1). Both specimens were tested using the tensile frame. Although both specimens were tested with different optical systems and DIC patterns, the strain behavior is similar (Fig. 13): it increases to approximately 0.03 mm/mm strain then suddenly decreases due to the onset of necking in each specimen. This shows that the internal fluorescent DIC pattern is capable, on average, of capturing internal deformation exhibited in the specimen, consistent with the surface deformation using more traditional DIC. Although the uncertainty of the measurements for internal DIC are larger than the traditional DIC in Fig. 13, this is most likely because (1) the translation frame on the wide-field microscope did not exhibit the issues seen in the fluorescent microscope positioning stage, and (2) the traditional surface pattern was closer to the optimal for the FOV and had better contrast. With further optimization of the internal fluorescent DIC pattern for one specific FOV, the uncertainty will be reduced and allow for the use of smaller subset sizes. These should allow for the internal fluorescent DIC pattern to be used for more local strain measurements as well.

Summary & Conclusions

A non-intrusive and non-disruptive internal fluorescent pattern was designed, developed, and tested for use with digital image correlation (DIC) to measure internal deformation at microscale levels in a polymer matrix. The internal fluorescent pattern was collimated through the thickness of the specimen and introduced through a UV photoactivatable patterning technique. The resulting pattern was visible with a laser scanning confocal microscope and detected on a secondary wide field microscope. This new patterning method is more amenable to applying internal patterns without introducing physical particles to the polymer specimen hence preventing significant changes to the mechanical properties of the material.

The capability of the internal fluorescent pattern for DIC measurement was confirmed and quantified through a series of assessments including noise-floor, rigid body motion, and various uniaxial tests. At this point in development of this method, the pattern scale was not optimized for spatial resolution; therefore, the DIC parameter study was used to select a single set of DIC analysis parameters that would minimize the uncertainty while using the smallest overall length for strain measurement considering the sub-optimum pattern scale. The resulting subset, step, and filter sizes were used throughout the work.

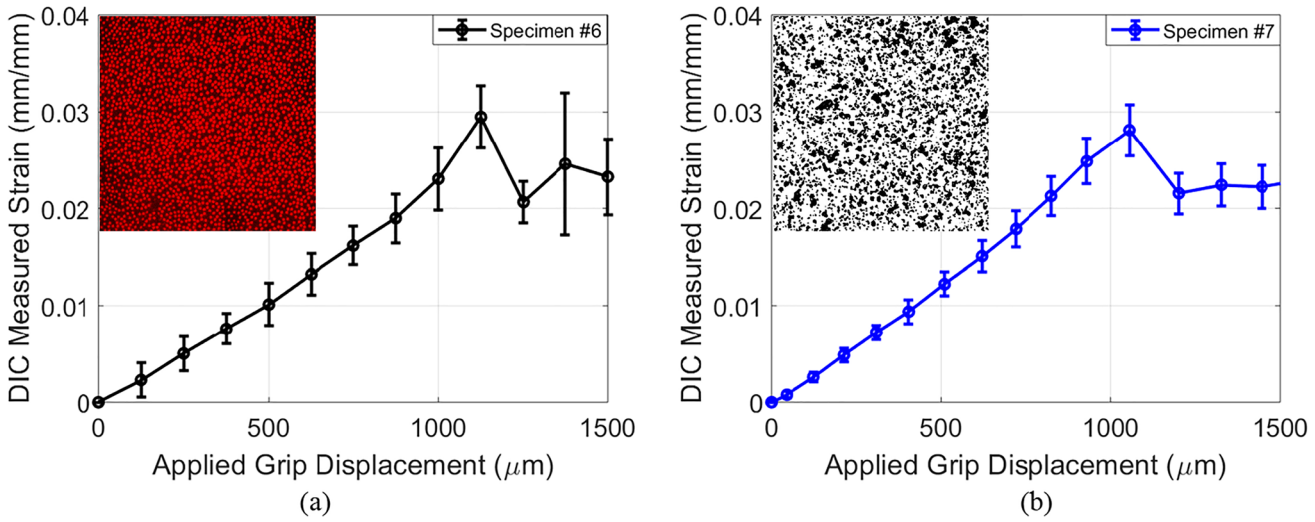

Fig. 13 Comparison of average true strain for *Tensile Experiment 3* using two different DIC patterning methods; (**a**) internal fluorescent UV activated pattern (inset) observed with a 10×magnification. The standard deviations are 0.0036 mm/mm strain on average (**b**) surface airbrush spray-painted pattern (inset) observed with a 4×magnification. The standard deviations are 0.0014 mm/mm strain on average

An existing method of DIC calibration for standard optical microscopes, combining a linear scaling and a non-linear image correction, was applied and rigorously assessed. The linear scaling (image scale) was assumed to be constant with changes in depth. This assumption was found to be acceptable based on the intended use (i.e., strain measurement) and the rigid body motion test results; however, for more detailed use of the displacement measurements, further investigation should be performed. The non-linear distortion correction had a different structure in the *X* and *Y* directions of the image, likely due to the laser raster resulting in a drift-like distortion. The non-linear distortion correction did not seem to vary substantially with depth, and it was determined that the distortion correction for the near-surface layer could be used at all the deeper layers being measured. This was confirmed by noise-floor results showing a minor difference when assessed with the near-surface layer correction rather than layer specific corrections.

The spatial noise-floor assessment showed strain uncertainty of about 0.0003 mm/mm at 40 μm depth, and the uncertainty increased slightly with depth. The rigid body motion, or extended noise-floor assessment, showed a less than two-fold increase from the static noise-floor in strain uncertainty. However, with the tensile frame the rigid body noise floor was about 3 times larger than the static noise floor with the tensile frame. Additionally, the spatial and temporal noise-floors performed with the tensile frame showed similar magnitudes between the temporal and spatial results. Comparing the noise floor with and without the tensile frame, showed that the tensile frame increases the static noise floor by a factor of 3 and increased the rigid body motion noise floor by a factor of 6. The increase in uncertainty when using the tensile frame was traced back to the inability of the fluorescent microscope positioning stage to hold position with the weight of the tensile frame. At the time, this was the only positioning stage and microscope available to image the fluorescent pattern, so unfortunately, this increased level of uncertainty had to be tolerated for the tensile uniaxial tests that were performed. The mean values of all the noise-floors showed a negative strain bias in the *Y*-direction, and this was presumed to be a result of the non-linear distortion aspect of the calibration that is related to the laser raster.

Regarding the non-intrusive and non-disruptive nature of this patterning and imaging technique, *Tensile Experiment 1* demonstrated that the addition of the dye to create the internal pattern did not affect the macro mechanical behavior of the transparent polymer material. Additionally, *Tensile Experiment 3* demonstrated that the spatial average strains determined using the internal DIC compared well with the more traditional surface DIC, with the internal DIC only slightly increasing the strain uncertainty. To assess that the strain measured at deeper layers would not be affected by the deformation or lack of deformation in the layers being imaged through, two tests, *Tensile Experiment 2*, were performed with a stack of two specimens with a single one deforming. The first test had the top specimen deforming and the bottom specimen not deforming, and the second test had the top and bottom specimens reversed. The results show that imaging through a specimen (deforming or not) did not seem to bias the measurement of the bottom specimen, but the bottom specimen did show increased strain uncertainty. It was also shown that the use of zero-normalized sum of square differences (ZNSSD) as the correlation criterion did seem to reduce the strain uncertainty in the bottom specimen compared to the use of normalized sum of square differences (NSSD) as the correlation criterion. This improvement was only seen for the bottom specimen results, whereas the top specimen showed little to no change in uncertainty using either correlation criterion. It seemed that some of the additional uncertainty was due to the airgap that unfortunately occurred between the top and bottom specimens.

Based on these results, it has been shown that this new non-intrusive and non-disruptive method of DIC patterning can measure strain fields on sub-surface planes in a transparent polymer matrix, without bias from material deformation above that plane. It was also found that after correcting some experimental limitations (e.g., increased microscope positioning stage weight capacity and improved lighting conditions) the uncertainties should be substantially reduced. Now that the patterning method has shown its functionality, the pattern size can be optimized for the intended field of view and the pattern application optimized for the required depths of interest within the material.

Disclaimer

Certain commercial equipment, instruments, or materials are identified in this paper in order to specify the experimental procedure adequately. Such identification is not intended to imply recommendation or endorsement by the National Institute of Standards and Technology, nor is it intended to imply that the materials or equipment identified are necessarily the best available for the purpose.

Supplementary Information The online version contains supplementary material available at https://doi.org/10.1007/s40799-023-00628-2.

Acknowledgements The authors would like to thank Joy Dunkers and the Biological Division at NIST for providing optical microscopy support, Christopher Amigo, Edward Pompa, and Travis Shatzley for providing manufacturing and polishing support. We would like to also thank Dean DeLongchamp, Joseph Kline, Gale Holmes, and Christopher Soles for helpful comments and suggestions regarding this study. We would also like to thank Hubert Schreier of Correlated Solutions Inc. for assistance in visualizing the 2D-DIC calibration pixel mapping.

Data Availability The datasets plotted in this article and supplementary material file are freely available at [DOI: https://doi.org/10.18434/mds2-2929]. For access to any of the underlying data to these results (e.g., calibration image files), please contact the corresponding authors mark.iadicola@nist.gov or louise.ahurepowell@nist.gov.

Declarations

Declaration of interests The authors declare that they have no known competing financial interests or personal relationships that could have appeared to influence the work reported in this paper.

References

1. Fitzer E (1989) Pan-based carbon fibers—present state and trend of the technology from the viewpoint of possibilities and limits to influence and to control the fiber properties by the process parameters. Carbon 27:621–645. https://doi.org/10.1016/0008-6223(89)90197-8
2. Gupta MK, Srivastava RK (2016) Mechanical properties of hybrid fibers-reinforced polymer composite: a review. Polym-Plast Technol Eng 55:626–642. https://doi.org/10.1080/03602559.2015.1098694
3. Koniuszewska AG, Kaczmar JW (2016) Application of polymer based composite materials in transportation. Prog Rubber Plast Recycl Technol 32:1–24. https://doi.org/10.1177/147776061603200101
4. Chukov D, Nematulloev S, Torokhov V et al (2019) Effect of carbon fiber surface modification on their interfacial interaction with polysulfone. Results Phys 15:102634. https://doi.org/10.1016/j.rinp.2019.102634
5. Unterweger C, Brüggemann O, Fürst C (2014) Synthetic fibers and thermoplastic short-fiber-reinforced polymers: properties and characterization. Polym Compos 35:227–236. https://doi.org/10.1002/pc.22654
6. Jabbar SA, Farid SBH (2018) Replacement of steel rebars by GFRP rebars in the concrete structures. Karbala Int J Mod Sci 4:216–227. https://doi.org/10.1016/j.kijoms.2018.02.002
7. Yang Y, Sun P, Nagarajaiah S et al (2017) Full-field, high-spatial-resolution detection of local structural damage from low-resolution random strain field measurements. J Sound Vib 399:75–85. https://doi.org/10.1016/j.jsv.2017.03.016
8. Bowman KB, Mollenhauer DH (2002) Experimental investigation of residual stresses in layered materials using moire´ interferometry. J Electron Packag 124:340–344. https://doi.org/10.1115/1.1497627
9. Tobey RI, Siemens ME, Cohen O et al (2007) Ultrafast extreme ultraviolet holography: dynamic monitoring of surface deformation. Opt Lett 32:286. https://doi.org/10.1364/OL.32.000286
10. Løkberg OJ (1987) Electronic Speckle Pattern Interferometry. In: Soares ODD (ed) Optical Metrology. Springer Netherlands, Dordrecht, pp 542–572
11. Mashiwa N, Furushima T, Manabe K (2017) Novel non-contact evaluation of strain distribution using digital image correlation with laser speckle pattern of low carbon steel sheet. Procedia Eng 184:16–21. https://doi.org/10.1016/j.proeng.2017.04.065
12. Berfield TA, Patel JK, Shimmin RG et al (2007) Micro- and nanoscale deformation measurement of surface and internal planes via digital image correlation. Exp Mech 47:51–62. https://doi.org/10.1007/s11340-006-0531-2
13. Jones EMC, Silberstein MN, White SR, Sottos NR (2014) In situ measurements of strains in composite battery electrodes during electrochemical cycling. Exp Mech 54:971–985. https://doi.org/10.1007/s11340-014-9873-3
14. Valenza A, Fiore V, Fratini L (2011) Mechanical behaviour and failure modes of metal to composite adhesive joints for nautical applications. Int J Adv Manuf Technol 53:593–600. https://doi.org/10.1007/s00170-010-2866-1
15. Croom B, Wang W-M, Li J, Li X (2016) Unveiling 3D deformations in polymer composites by coupled micro x-ray computed tomography and volumetric digital image correlation. Exp Mech 56:999–1016. https://doi.org/10.1007/s11340-016-0140-7
16. Hardiman M, Vaughan TJ, McCarthy CT (2017) A review of key developments and pertinent issues in nanoindentation testing of fibre reinforced plastic microstructures. Compos Struct 180:782–798. https://doi.org/10.1016/j.compstruct.2017.08.004
17. Koerber H, Xavier J, Camanho PP (2010) High strain rate characterisation of unidirectional carbon-epoxy IM7-8552 in transverse compression and in-plane shear using digital image correlation. Mech Mater 42:1004–1019. https://doi.org/10.1016/j.mechmat.2010.09.003
18. Sisakht Mohsen R, Saied NK, Ali Z et al (2009) Theoretical and experimental determination of tensile properties of nanosized and micron-sized $CaCO_3$ /PA66 composites. Polym Compos 30:274–280. https://doi.org/10.1002/pc.20602
19. Zare Y, Rhee KY, Hui D (2017) Influences of nanoparticles aggregation/agglomeration on the interfacial/interphase and tensile properties of nanocomposites. Compos Part B Eng 122:41–46. https://doi.org/10.1016/j.compositesb.2017.04.008
20. Franck C, Hong S, Maskarinec SA et al (2007) Three-dimensional full-field measurements of large deformations in soft materials using confocal microscopy and digital volume correlation. Exp Mech 47:427–438. https://doi.org/10.1007/s11340-007-9037-9
21. Mehdikhani M, Aravand M, Sabuncuoglu B et al (2016) Full-field strain measurements at the micro-scale in fiber-reinforced composites using digital image correlation. Compos Struct 140:192–201. https://doi.org/10.1016/j.compstruct.2015.12.020
22. Seethamraju S, Obrzut J, Douglas JF et al (2020) Quantifying fluorogenic dye hydration in an epoxy resin by noncontact microwave dielectric spectroscopy. J Phys Chem B 124:2914–2919. https://doi.org/10.1021/acs.jpcb.9b11622
23. Coimbatore Balram K, Westly DA, Davanco MI et al (2016) The nanolithography toolbox. J Res Natl Inst Stand Technol 121:464. https://doi.org/10.6028/jres.121.024
24. International Digital Image Correlation Society, Jones E, Iadicola M, et al (2018) A Good Practices Guide for Digital Image Correlation. International Digital Image Correlation Society
25. Qian W, Li J, Zhu J et al (2020) Distortion correction of a microscopy lens system for deformation measurements based on speckle pattern and grating. Opt Lasers Eng 124:105804. https://doi.org/10.1016/j.optlaseng.2019.105804
26. Correlated Solution, Inc, Application Note AN-610 using microscope distortion correction in Vic-2D
27. Schreier HW, Garcia D, Sutton MA (2004) Advances in light microscope stereo vision. Exp Mech 44:278–288. https://doi.org/10.1007/BF02427894
28. Schreier HW, Sutton MA (2006) Calibrated sensor and method for calibrating same. US Patent, 7133570 B1: 1–10
29. Sutton MA, Li N, Joy DC et al (2007) Scanning electron microscopy for quantitative small and large deformation measurements Part I: SEM imaging at magnifications from 200 to 10,000. Exp Mech 47:775–787. https://doi.org/10.1007/s11340-007-9042-z
30. Kammers AD, Daly S (2013) Digital image correlation under scanning electron microscopy: methodology and validation. Exp Mech 53:1743–1761. https://doi.org/10.1007/s11340-013-9782-x
31. Virtanen P, Gommers R, Oliphant TE et al (2020) SciPy 1.0: fundamental algorithms for scientific computing in Python. Nat Methods 17:261–272. https://doi.org/10.1038/s41592-019-0686-2